

Article

# Pressure Dependence of Structural and Mechanical Properties of Single-Crystal Tungsten: A Molecular Dynamics Study

Xuepeng Liu <sup>1,2,\*</sup> , Kezhong Xu <sup>1,2</sup> and Hua Zhai <sup>1,2,\*</sup>

<sup>1</sup> Anhui Province Key Lab of Aerospace Structural Parts Forming Technology and Equipment, Institute of Industry and Equipment Technology, Hefei University of Technology, Hefei 230009, China; xukezhong@mail.hfut.edu.cn

<sup>2</sup> School of Mechanical Engineering, Hefei University of Technology, Hefei 230009, China

\* Correspondence: liuxuepeng@hfut.edu.cn (X.L.); jxzhaihuajx@hfut.edu.cn (H.Z.)

**Abstract:** In the current study, molecular dynamics (MD) simulations were performed to study the pressure dependence of the structural and mechanical properties of single-crystal tungsten. The results show that single-crystal tungsten possesses noteworthy high-pressure stability and exhibits linear lattice contraction with increasing external pressure. Consistent with the results of the performed experiments, the predicted elastic moduli, including Young's modulus, shear modulus, and bulk modulus, as well as Poisson's ratio and Pugh's modulus ratio, show a clear increasing trend with the increase in pressure. Under uniaxial tensile loading, the single-crystal tungsten at high pressures experiences a phase transition from BCC to FCC and other disordered structures, which results in a stripe-like morphology in the tungsten crystal. These results are expected to deepen our understanding of the high-pressure structural and mechanical behaviors of tungsten materials.

**Keywords:** high pressure; structure; mechanical properties; tungsten; molecular dynamics simulation



**Citation:** Liu, X.; Xu, K.; Zhai, H. Pressure Dependence of Structural and Mechanical Properties of Single-Crystal Tungsten: A Molecular Dynamics Study. *Metals* **2021**, *11*, 1898. <https://doi.org/10.3390/met11121898>

Academic Editors: Alberto Moreira Jorge Junior and Carlos Capdevila-Montes

Received: 1 September 2021  
Accepted: 24 November 2021  
Published: 25 November 2021

**Publisher's Note:** MDPI stays neutral with regard to jurisdictional claims in published maps and institutional affiliations.



**Copyright:** © 2021 by the authors. Licensee MDPI, Basel, Switzerland. This article is an open access article distributed under the terms and conditions of the Creative Commons Attribution (CC BY) license (<https://creativecommons.org/licenses/by/4.0/>).

## 1. Introduction

Tungsten (W) is a body-centered cubic (BCC) rare metal (structured in  $Im\bar{3}m$ ), and it has the highest melting point (3680 K) of all the known elements [1]. Due to the advantages of its high melting point, high heat conductivity, high sputtering resistance, and superior mechanical strength [1–3], W and its alloys have wide application potential in aerospace, electronics, and chemical and national defense military industries [4–6]. Notably, tungsten is considered to be one of the most likely candidates for plasma-facing material to be used in future nuclear fusion reactors and for target material in spallation facilities due to its outstanding comprehensive advantages [7–10].

In recent years, the high-pressure behavior of tungsten has gained extensive attention due to its importance in the control of its electronic structure [11] and diamond anvil cell applications [12]. Numerous experimental and theoretical studies on the structural and elastic properties of tungsten under high pressures have been performed. The diamond anvil cell experiments [13] show that the BCC crystalline structure of tungsten remains stable up to an extremely high pressure of 153 GPa at room temperature. The high-pressure elastic properties of tungsten are commonly measured by utilizing ultrasonic interferometry techniques. The first effort may have been made by Katahara et al. [14], who measured the elastic moduli of tungsten at pressures up to 0.5 GPa. With the development of measurement techniques, Qi et al. [15] recently studied the elastic constants and Poisson's ratio of tungsten and their pressure dependence under pressures up to 13 GPa. Simultaneously, the high-pressure elastic moduli of tungsten were also predicted by using first-principles calculations with the assumption that the temperature of the system approaches absolute zero [16,17]. Despite the numerous investigations discussed above, a systematic study of the structural and mechanical properties of tungsten under high pressures has not yet been

conducted. In particular, to date, very little is known about the high-pressure dynamical response of tungsten under tensile loading due to limitations in experimental conditions.

Molecular dynamics (MD) simulation is an effective tool that can be used to study the structural and mechanical performance of metal materials. The advantage of using this tool is that it allows the systematic and rapid exploration of both the material parameters and system size, as well as the laboratory conditions (temperature, pressure, and irradiation). In addition, the MD calculation is capable of directly observing the detailed structural evolution that relies on data at the atomic level, which are difficult to obtain in conventional experiments. Such simulations have been successfully used to predict the elastic and mechanical properties of tungsten crystal under high-temperature [18,19] and plasma-exposed conditions [20,21]. However, to the best of our knowledge, there is a scarcity of atomistic MD simulation research on the structural and mechanical properties of single-crystal tungsten under high-pressure conditions.

In this paper, we perform a systematic investigation of the high-pressure structural and mechanical properties of single-crystal tungsten by using atomistic MD simulations. The remainder of this article is organized as follows: in Section 2, we describe the details of the atomistic model and computational methods; the results and discussion are given in Section 3; and the conclusions of this work are drawn in Section 4.

## 2. Model and Methods

### 2.1. Simulation Details

The simulations in the present work were performed using the large-scale atomic/molecular massively parallel simulator (LAMMPS) (Sandia National Laboratories, Albuquerque, NM, USA) [22], which is a classical molecular dynamics (MD) code for material modeling and simulation. The unit cell of the single-crystal tungsten, as displayed in the left panel of Figure 1, is a body-centered cubic (BCC) crystal structure with a lattice constant of  $a = 3.165 \text{ \AA}$ . The X, Y, and Z coordinate axes are aligned along the [100], [010], and [001] orientations of the BCC crystal, respectively. In this work, a supercell with a size of  $20 a \times 20 a \times 20 a$  was constructed by repeating the BCC unit cell along the [001], [010], and [100] directions of the crystal (see the right panel of Figure 1). Periodic boundary conditions were applied in all three directions to determine the bulk properties compared with experimental data in the literature [15]. The quality of the interatomic potential is of vital importance for modeling in MD simulations. In this study, a modified embedded potential developed by Zhou et al. [23] was utilized to simulate the structural and mechanical properties of single-crystal tungsten under high pressures. The modified embedded atom potential function is given by:

$$U = \frac{1}{2} \sum_{i,j \neq i} \phi_{ij}(r_{ij}) + \sum_i F_i(\rho_i) \quad (1)$$

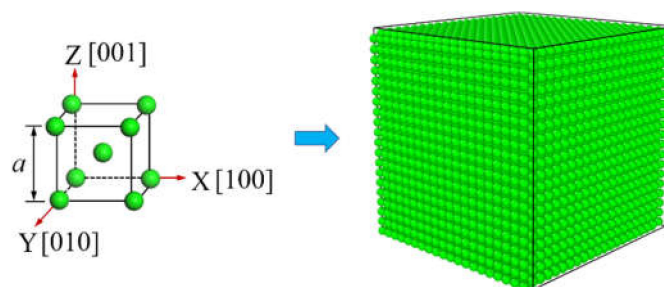


**Figure 1.** A BCC unit cell with a lattice parameter of  $a = 3.165 \text{ \AA}$  (left panel) and a schematic representation of a cubic single tungsten crystal with a size of  $20 a \times 20 a \times 20 a$  based on the BCC unit cell (right panel).

where  $\phi_{ij}(r_{ij})$  is the pair energy between atoms  $i$  and  $j$  spaced by a distance of  $r_{ij}$ , and  $F_i$  is the correction term, which stands for the embedded energy of the atom  $i$  embedding into a local site with an electron density  $\rho_i$ .

To obtain an equilibrium structure of single-crystal tungsten before loading, the energy of the system was firstly minimized using the conjugate gradient algorithm. Then, additional simulation annealing under the desired hydrostatic pressure was performed for 10 ps at a temperature of 300 K in the NPT ensemble (constant number of atoms, pressure, and temperature). After this relaxation, the equilibrated structure of single-crystal tungsten was subjected to different loading modes (uniaxial tension, pure shear, and hydrostatic compression) under the NPT ensemble. The NPT ensemble was adopted to simulate different loading schemes of the single-crystal tungsten, because it is capable of taking into account the pressure of the system. To investigate the pressure effect, the cubic single-crystal tungsten was deformed under different pressures  $P$  in a wide range of 0–16 GPa. Unless otherwise stated, all the simulations were conducted at a temperature of 300 K, and a time step of 1.0 fs was selected. All of the simulation snapshots were generated using the open-source software OVITO (Open Visualization Tool) [24]. The stresses at the atomic level were calculated using the Virial theorem [25], which is defined by

$$\mathbf{T} = -\frac{1}{V} \left( \sum_i m_i \mathbf{v}_i \otimes \mathbf{v}_i + \sum_i \sum_{j \neq i} \mathbf{F}_{ij} \otimes \mathbf{r}_{ij} \right), \quad (2)$$

where  $\mathbf{T}$  denotes the stress tensor;  $m$  represents the mass of the atom;  $V$  stands for the volume of the system; and  $\mathbf{r}$ ,  $\mathbf{v}$ , and  $\mathbf{F}$  are the location, velocity, and force vectors, respectively.

## 2.2. Computational Method of Elastic Modulus and Poisson's Ratio

When a material is deformed at the linear elastic stage, the stress ( $\sigma$ )–strain ( $\epsilon$ ) relationship of the material can be expressed by  $\sigma = E\epsilon$ , where  $E$  is the elastic modulus of the material. In order to obtain the Young's modulus ( $Y$ ) and shear modulus ( $G$ ) of the single-crystal tungsten, the as-prepared equilibrated configuration needs to be deformed under a uniaxial and a shear strain, independently. To compute the Young's modulus, the tungsten crystal was uniaxially stretched along the X direction (i.e., the [100] direction), as shown in Figure 2a. To calculate the shear modulus, the tungsten crystal was subjected to quasi-static shear loading in the [110] direction (see Figure 2b). For both cases, a constant strain rate of  $1 \times 10^7 \text{ s}^{-1}$  was selected. Then, the Young's and shear modulus of the single-crystal tungsten were derived from the slope in the linear regime of the tensile and shear stress–strain curves, respectively.

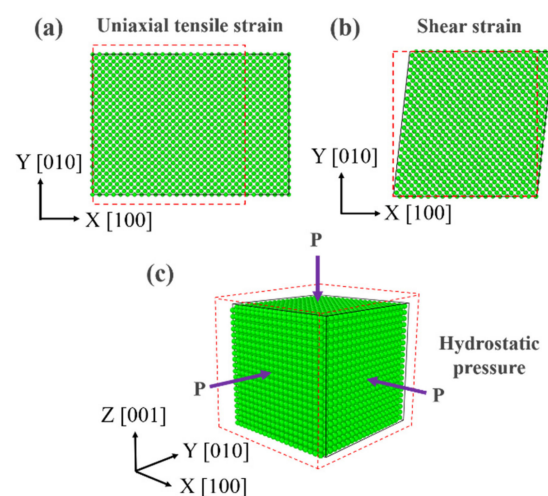


**Figure 2.** Schematic maps of (a) uniaxial tension, (b) shear deformation, and (c) hydrostatic compression of the cubic single-crystal tungsten.

The bulk modulus  $B$  reflects the resistance of a material to hydrostatic compression, which is defined by the ratio of the increase in infinitesimal pressure to the resulting relative decrease in the volume. It follows that  $B = -VdP/dV$ , in which  $P$  is the applied external pressure, and  $V$  is the initial volume of the material before applying the load. Based on its definition, the bulk modulus was obtained by incrementally and uniformly applying increased strain in three axial directions (see Figure 2c) and computing the resulting pressure  $P$ , which is equivalent to the negative diagonal elements of the stress tensor.

Poisson's ratio ( $\nu$ ) describes the deformation in the material in a direction perpendicular to the direction of the applied load. It is defined as the ratio of transverse strain to axial strain when the material is stretched or compressed along only one direction (for example, the X axis):

$$\nu = -\frac{\varepsilon_{trans}}{\varepsilon_{axial}} = -\frac{\varepsilon_y}{\varepsilon_x} = -\frac{\varepsilon_z}{\varepsilon_x} \quad (3)$$

where  $\varepsilon_{trans}$  is the transverse strain and  $\varepsilon_{axial}$  is the axial strain. To obtain Poisson's ratio, we calculated the linear strain of the single-crystal tungsten in the X and Y directions when it was stretched along the X axis. Then, Poisson's ratio could be achieved according to Equation (3).

### 3. Results and Discussion

#### 3.1. Dependence of Structural Properties on Pressure

To investigate the pressure dependence of the structural properties of single-crystal tungsten, a series of simulation runs were carried out for cubic crystal tungsten at different hydrostatic pressures. Figure 3 presents the simulation snapshots of the cubic single-crystal tungsten under different pressures at room temperature. Upon an increase in hydrostatic pressure from 0 to 16 GPa, the BCC crystalline structure of the single-crystal tungsten remained stable, and this was confirmed by the radial distribution function calculation (see the bottom panels in Figure 3). Such noteworthy high-pressure stability up to 16 GPa is consistent with previous experimental observations [13].

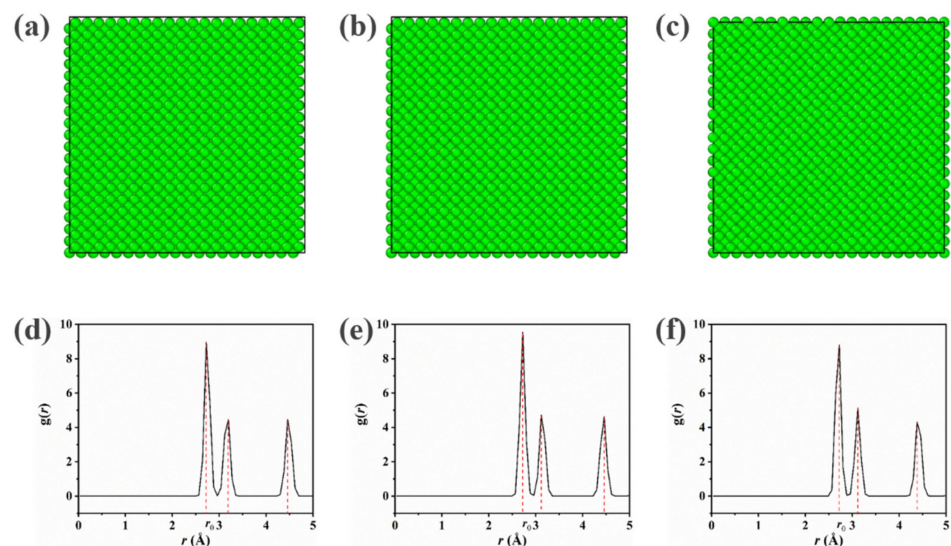


**Figure 3.** Equilibrated configurations of single-crystal tungsten under different hydrostatic pressures: (a) 0 GPa, (b) 8 GPa, and (c) 16 GPa. The corresponding radial distribution functions of single-crystal tungsten under different hydrostatic pressures: (d) 0 GPa, (e) 8 GPa, and (f) 16 GPa. Dotted lines in each panel represent the first three peaks of the radial distribution function. The first three peaks are located at the positions of  $r/r_0 = 1, \sqrt{4/3}, \sqrt{8/3}$  ( $r_0$  is the radius of the first coordination shell in the radial distribution function calculation), which means that the crystal structures are perfect BCC crystals.

To quantify the structural change in the single-crystal tungsten during the hydrostatic compression process, we calculated the lattice constant  $a$ , i.e., the  $2/\sqrt{3}$  center-to-center nearest neighbor distance for a BCC crystal, as a function of external pressure. Figure 4 shows the evolution of the lattice constant of the single-crystal tungsten with the increase in pressure. It can be seen that the lattice constant decreases linearly at the rate of  $\sim 0.0029$  Å per GPa of the applied pressure. This indicates that the structure of single-crystal tungsten tends to be more densely compacted upon hydrostatic compression.

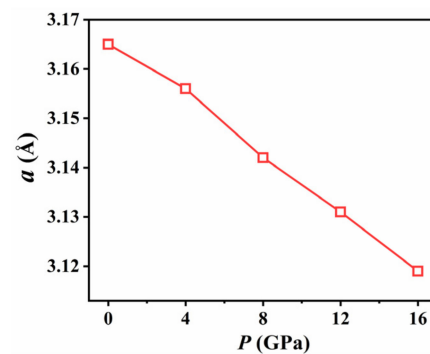


**Figure 4.** Lattice constants of the single-crystal tungsten at different pressures.

### 3.2. Role of Pressure in Elastic Properties

To identify the role of pressure in the elastic modulus of single-crystal tungsten, a series of MD simulations were carried out for a cubic crystal tungsten under different hydrostatic pressures in a wide range of 0–16 GPa. Figure 5a–c display the variations in the calculated Young’s, shear, and bulk moduli of the single-crystal tungsten as a function of pressure, respectively. It can be seen from Figure 5a that the Young’s modulus  $Y$  monotonically increased from 366 to 394 GPa with the increase in external pressure from 0 to 16 GPa. The results in Figure 5b show that the shear modulus  $G$  ranged from 160 to 186 GPa and increased linearly at the rate of  $\sim 1.6$  GPa per GPa of the external pressure. Figure 5c illustrates that the bulk modulus  $B$  varied in the range of 300–374 GPa, rising almost linearly with the increase in applied pressure. The predicted trends and values of Young’s, shear, and bulk moduli agree well with the experimental work of Qi et al. [15], who observed that the shear and bulk moduli of polycrystalline tungsten both increase monotonically with an increase in pressure. Obviously, the higher the external pressure, the closer the distance between atoms (see Figure 4) and the more densely compacted the lattice structure. Consequently, the single-crystal tungsten tends to be barely deformed at high pressure and thus leads to an enhanced elastic modulus.

Besides the elastic modulus, Poisson’s ratio  $\nu$  and Pugh’s modulus ratio (i.e., the ratio of bulk modulus to shear modulus,  $B/G$ ) are two other important parameters to consider when examining the mechanical performance of structural materials. On the basis of the current simulation data, the Poisson’s ratio and Pugh’s modulus ratio of single-crystal tungsten under high-pressure conditions were also investigated. Figure 6a gives the Poisson’s ratio  $\nu$  of a cubic, single-crystal tungsten under different pressures. It is shown that the Poisson’s ratio of the single-crystal tungsten increased from 0.284 to 0.325 at the highest applied pressure of 16 GPa. The computed Poisson’s ratio was within the normal range (from 0.27 to 0.42 [26]) of metal materials and showed a clear increase with an increase in pressure, which agrees reasonably with previous experiments [15]. Pugh’s modulus ratio  $B/G$  is a useful parameter to describe the ductility/brittleness of a solid material. According to Pugh’s criterion [27], a material with  $B/G$  larger than 1.75 is ductile, and that with  $B/G$  less than 1.75 tends to be brittle. Pugh’s modulus ratios of single-crystal tungsten as a function of pressure are plotted in Figure 6b. It can be seen that the calculated Pugh’s modulus ratio of single-crystal tungsten at 0 GPa is 1.88, implying that single-crystal tungsten exhibits a ductile property at ambient conditions. With the increase in pressure, the Pugh’s modulus ratio became larger, which suggests that single-crystal tungsten becomes more ductile at higher pressures.

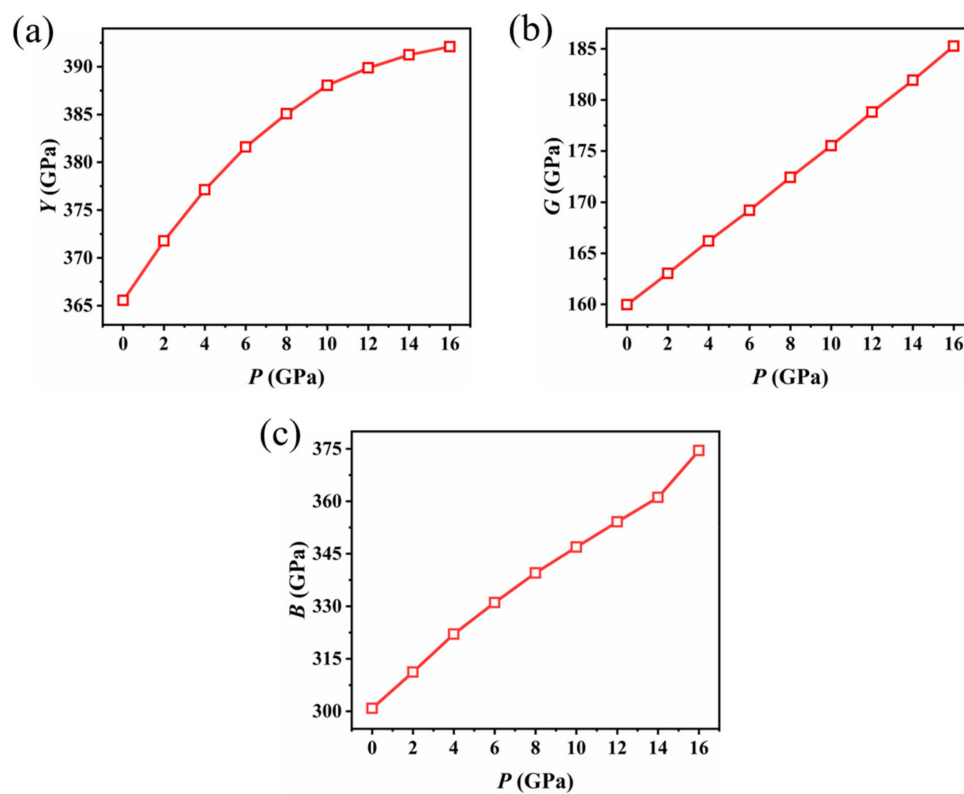


**Figure 5.** (a) Young's modulus, (b) shear modulus, and (c) bulk modulus of bulk single-crystal tungsten as a function of pressure.

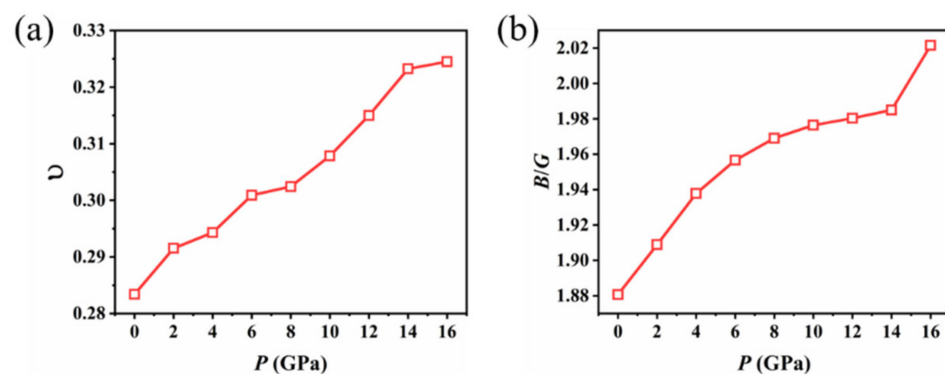


**Figure 6.** (a) Poisson's ratio and (b) Pugh's modulus ratio of single-crystal tungsten as a function of pressure.

The above computations of elastic properties are focused on the single-crystal tungsten with the same system size of  $20 a \times 20 a \times 20 a$  and the same strain rate of  $1 \times 10^7 \text{ s}^{-1}$ , and it is unclear whether the system size and strain rate affect the computational results. For this reason, simulations were conducted for different system sizes and strain rates to investigate the dependence of the elastic properties on these two parameters. The results in Tables 1 and 2 demonstrate that the Young's modulus, shear modulus, bulk modulus, Poisson's ratio, and Pugh's modulus ratio show only minimal dependence on the system size and strain rate.

**Table 1.** Young's modulus, shear modulus, bulk modulus, and Poisson's ratio for tungsten crystal with different system sizes at pressure of 8 GPa.

Box Sizes (nm)	Young's Modulus (GPa)	Shear Modulus (GPa)	Bulk Modulus (GPa)	Poisson's Ratio
20 <i>a</i> × 20 <i>a</i> × 20 <i>a</i>	388.86	173.02	339.52	0.3024
25 <i>a</i> × 25 <i>a</i> × 25 <i>a</i>	388.78	172.85	339.73	0.3160
30 <i>a</i> × 30 <i>a</i> × 30 <i>a</i>	388.65	173.02	339.10	0.3088
35 <i>a</i> × 35 <i>a</i> × 35 <i>a</i>	388.70	172.50	338.94	0.3140

**Table 2.** Young's modulus, shear modulus, and Poisson's ratio of tungsten at different strain rates and pressure of 8 GPa.

Strain Rates (s <sup>-1</sup> )	Young's Modulus (GPa)	Shear Modulus (GPa)	Poisson's Ratio
1 × 10 <sup>7</sup>	388.86	173.02	0.3024
5 × 10 <sup>7</sup>	388.68	172.51	0.3159
10 × 10 <sup>7</sup>	388.60	173.45	0.3079
15 × 10 <sup>7</sup>	388.76	172.69	0.3084

### 3.3. Phase Transition during Tensile Process at Different Pressures

Figure 7a shows the stress–strain curves of a cubic single-crystal tungsten under uniaxial tension at different pressures, and the corresponding atomic configurations at different tensile strains are displayed in Figure 8. As shown in Figure 7a, all of the stress–strain curves are of analogous shapes but have different initial slopes and maximum stresses. In the initial stage of small strain, stress increased linearly with strain. At this stage, the whole system experienced elastic deformation, and the BCC lattice structure remained unchanged (see Figure 8). The yield strength is defined as the maximum stress of the stress–strain curve, and the variations in yield strength as a function of pressure are displayed in Figure 7b. It can be clearly observed that the yield strength of the single-crystal tungsten linearly increased with the increase in external pressure. Once the strain exceeded the yield strain, the metal tungsten began to show plastic deformation, and, as such, it was no longer a perfect crystal. At ambient conditions ( $P = 0$  GPa), we observed that the BCC structural atoms gradually transformed to the FCC structure with an increase in strain, which led to a band-like FCC region in the tungsten crystal (see Figure 8a). Similar BCC–FCC phase transition can be found in the case of atomistic simulations of BCC metal tantalum under tensile loading at ambient pressures [28]. In addition, MD simulations have also shown a phase transformation from BCC to body-centered tetragonal (BCT) for intermetallic NiAl nanowires under tensile loading [29,30]. Carefully observing the simulation snapshot in Figure 8a, one can see that there also exists a small amount of other disordered structures in the tungsten crystal. These disordered structures are mainly distributed at the BCC–FCC phase boundary. When the external pressure was raised to  $P = 8$  GPa, we also observed a phase transition in the tungsten crystal, as the strain was greater than the yield value. However, unlike the case of ambient pressure, the BCC structure at elevated pressures transformed into a mixture of FCC and other disordered structures, which finally led to a stripe-like morphology in the tungsten crystal (see b). The common neighbor analysis results in Figure 9b show that the ratios of the FCC and other disordered atoms are comparable in the system. At a higher pressure of  $P = 16$  GPa, a similar phase transition from BCC to FCC and other disordered structures was also observed. Comparing the common neighbor analysis results at pressures of 0, 8, and 16 GPa, it can be observed that the ratio of the FCC structure in the system decreased with the increase in pressure (see Figure 9a–c). This implies that increasing the pressure can effectively inhibit the occurrence of a BCC-to-FCC phase transition.

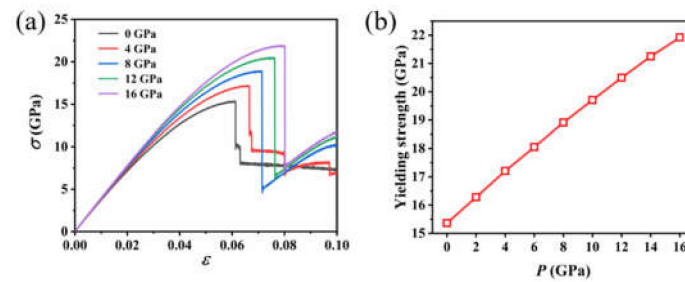


**Figure 7.** (a) Stress–strain curves of single-crystal tungsten under uniaxial tension at different pressures. (b) Yielding strength of single-crystal tungsten as a function of pressure.

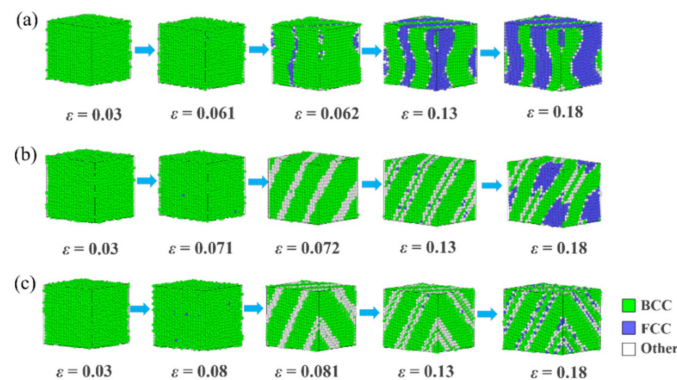


**Figure 8.** Atomic configurations of single-crystal tungsten at different strains during uniaxial tension in the presence of different pressures: (a) 0 GPa, (b) 8 GPa, and (c) 16 GPa.

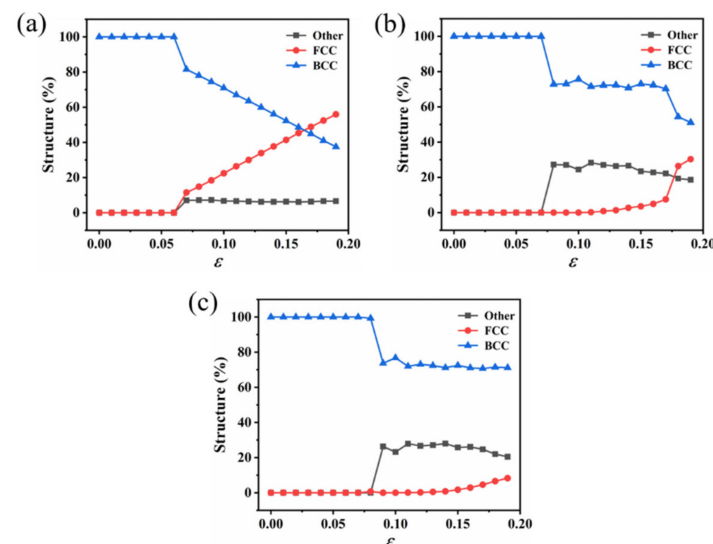


**Figure 9.** Ratios of BCC, FCC, and other disordered structures during uniaxial tension at different pressures: (a) 0 GPa, (b) 8 GPa, and (c) 16 GPa.

#### 4. Conclusions

In summary, we conducted MD simulations to systematically study the structural and mechanical properties of single-crystal tungsten under different hydrostatic pressures. Our computations show that the crystalline structure of the single crystal remains intact up to a high pressure of 16 GPa and exhibits linear lattice contraction with the increase in the applied pressure. Using linear regression analysis approaches, the elastic moduli of the single-crystal tungsten were calculated. It was found that the Young's modulus, shear modulus, and bulk modulus, as well as Poisson's ratio, show a clear increasing trend with

the increase in pressure, which is in good agreement with the experimental results [15]. In addition, the Pugh's modulus ratio of the single-crystal tungsten increases with the increase in pressure, implying that hydrostatic compression can effectively improve the ductility of BCC tungsten. Under uniaxial tensile deformation, the single-crystal tungsten at elevated pressures undergoes a phase transition from BCC to FCC and other disordered structures, which results in stripe-like morphology in the tungsten crystal. We hope that these findings provide a deeper understanding of the high-pressure structural and mechanical behaviors of tungsten materials.

**Author Contributions:** Conceptualization, X.L.; Data curation, K.X.; Funding acquisition, X.L.; Methodology, K.X.; Resources, H.Z.; Software, K.X. and H.Z.; Supervision, X.L. and H.Z.; Visualization, K.X.; Writing (original draft), K.X.; Writing (review and editing), X.L. and H.Z. All authors have read and agreed to the published version of the manuscript.

**Funding:** This research was funded by the National Natural Science Foundation of China (No. 11802081), the Fundamental Research Funds for the Central Universities of China (No. JZ2020HG7B0029), and the Anhui Province Key Project (No. 201903c08020008).

**Institutional Review Board Statement:** Not applicable.

**Informed Consent Statement:** Not applicable.

**Data Availability Statement:** The data generated and/or analyzed during the current study are not publicly available for legal/ethical reasons but are available from the corresponding author upon reasonable request.

**Acknowledgments:** The authors declare that all the support is covered by the author contribution or funding sections.

**Conflicts of Interest:** The authors declare no conflict of interest.

## References

1. Lassner, E.; Schubert, W.D. *The Element Tungsten*; Springer: New York, NY, USA, 1999; ISBN 978-1-4613-7225-7.
2. Zhang, T.; Deng, H.W.; Xie, Z.M.; Liu, R.; Xie, Z.M.; Yang, J.F.; Liu, C.S.; Wang, X.P.; Fang, Q.F.; Xiong, Y. Recent progresses on designing and manufacturing of bulk refractory alloys with high performances based on controlling interfaces. *J. Mater. Sci. Technol.* **2020**, *52*, 29–62. [[CrossRef](#)]
3. Rieth, M.; Doerner, R.; Hasegawa, A.; Ueda, Y.; Wirtz, M. Behavior of tungsten under irradiation and plasma interaction. *J. Nucl. Mater.* **2019**, *519*, 334–368. [[CrossRef](#)]
4. Manikandan, N.; Arulkirubakaran, D.; Palanisamy, D.; Raju, R. Influence of wire-EDM textured conventional tungsten car-bide inserts in machining of aerospace materials (Ti–6Al–4V alloy). *Mater. Manuf. Processes* **2019**, *34*, 103–111. [[CrossRef](#)]
5. Sonar, T.; Malarvizhi, S.; Balasubramanian, V. Influence of arc constriction current frequency on tensile properties and microstructural evolution of tungsten inert gas welded thin sheets of aerospace alloy. *Trans. Nonferrous Met. Soc. China* **2021**, *31*, 456–474. [[CrossRef](#)]
6. Li, Y.; Niu, J.; Xue, T.; Duan, X.; Tian, Q.; Wen, Y.; Lu, X.; Xu, J.; Lai, L.; Chang, Y.; et al. Multifunctional Porous Nanohybrid Based on Graphene-Like Tungsten Disulfide on Poly(3,4-ethoxylenedioxythiophene) for Supercapacitor and Electrochemical Nanosensing of Quercetin. *J. Electrochem. Soc.* **2020**, *167*, 047512. [[CrossRef](#)]
7. Philipps, V. Tungsten as material for plasma-facing components in fusion devices. *J. Nucl. Mater.* **2011**, *415*, S2–S9. [[CrossRef](#)]
8. Emmerich, T.; Qu, D.; Vaßen, R.; Aktaa, J. Development of W-coating with functionally graded W/EUROFER-layers for protection of First-Wall materials. *Fusion Eng. Des.* **2018**, *128*, 58–67. [[CrossRef](#)]
9. Yang, X.; Qiu, W.; Chen, L.; Tang, J. Tungsten–potassium: A promising plasma-facing material. *Tungsten* **2019**, *1*, 141–158. [[CrossRef](#)]
10. Heuer, S.; Coenen, J.W.; Pintsuk, G.; Matějček, J.; Vilémová, M.; Linsmeier, C. Overview of challenges and developments in joining tungsten and steel for future fusion reactors. *Phys. Scr.* **2020**, *T171*, 014028. [[CrossRef](#)]
11. Jiang, D.; Zhong, S.; Xiao, W.; Liu, D.; Wu, M.; Liu, S. Structural, mechanical, electronic, and thermodynamic properties of pure tungsten metal under different pressures: A first-principles study. *Int. J. Quantum. Chem.* **2020**, *120*, e26231. [[CrossRef](#)]
12. Yan, J.; Doran, A.; MacDowell, A.A.; Kalkan, B. A tungsten external heater for BX90 diamond anvil cells with a range up to 1700 K. *Rev. Sci. Instrum.* **2021**, *92*, 013903. [[CrossRef](#)]
13. Dewaele, A.; Loubeyre, P.; Mezouar, M. Equations of state of six metals above 94 GPa. *Phys. Rev. B* **2004**, *70*, 094112. [[CrossRef](#)]
14. Katahara, K.W.; Manghnani, M.H.; Fisher, E.S. Pressure derivatives of the elastic moduli of BCC Ti–V–Cr, Nb–Mo and Ta–W alloys. *J. Phys. F Met. Phys.* **1979**, *9*, 773–790. [[CrossRef](#)]

15. Qi, X.; Cai, N.; Chen, T.; Wang, S.; Li, B. Experimental and theoretical studies on the elasticity of tungsten to 13 GPa. *J. Appl. Phys.* **2018**, *124*, 075902. [[CrossRef](#)]
16. Koči, L.; Ma, Y.; Oganov, A.R.; Souvatzis, P.; Ahuja, R. Elasticity of the superconducting metals V, Nb, Ta, Mo, and W at high pressure. *Phys. Rev. B* **2008**, *77*, 214101. [[CrossRef](#)]
17. Vekilov, Y.K.; Krasilnikov, O.M.; Lugovskoy, A.V.; Lozovik, Y.E. Higher-order elastic constants and megabar pressure effects of bcc tungsten: Ab initio calculations. *Phys. Rev. B* **2016**, *94*, 104114. [[CrossRef](#)]
18. Ma, B.; Rao, Q.; He, Y. Molecular dynamics simulation of temperature effect on tensile mechanical properties of single crystal tungsten nanowire. *Comput. Mater. Sci.* **2016**, *117*, 40–44. [[CrossRef](#)]
19. Chang, H.; Huang, Z.; Wen, S.; Chen, J.M.; Liu, X.; Pan, M.; Zhao, Y. The influence of crystal defects on the elastic properties of tungsten metals. *Fusion Eng. Des.* **2016**, *109–111*, 321–325. [[CrossRef](#)]
20. Kobayashi, R.; Hattori, T.; Tamura, T.; Ogata, S. A molecular dynamics study on bubble growth in tungsten under helium irradiation. *J. Nucl. Mater.* **2015**, *463*, 1071–1074. [[CrossRef](#)]
21. Weerasinghe, A.; Wirth, B.D.; Maroudas, D. Elastic Properties of Plasma-Exposed Tungsten Predicted by Molecular-Dynamics Simulations. *ACS Appl. Mater. Interfaces* **2020**, *12*, 22287–22297. [[CrossRef](#)]
22. Plimpton, S. Fast Parallel Algorithms for Short-Range Molecular Dynamics. *J. Comput. Phys.* **1995**, *117*, 1–19. [[CrossRef](#)]
23. Zhou, X.W.; Wadley, H.N.G.; Johnson, R.A.; Larson, D.J.; Tabat, N.; Cerezo, A.; Petford-Long, A.K.; Smith, G.D.W.; Clifton, P.H.; Martens, R.L.; et al. Atomic scale structure of sputtered metal multilayers. *Acta Mater.* **2001**, *49*, 4005–4015. [[CrossRef](#)]
24. Stukowski, A. Visualization and analysis of atomistic simulation data with OVITO—the Open Visualization Tool. *Model. Simul. Mater. Sci. Eng.* **2010**, *18*, 015012. [[CrossRef](#)]
25. Nielsen, O.H.; Martin, R.M. Quantum-mechanical theory of stress and force. *Phys. Rev. B* **1985**, *32*, 3780–3791. [[CrossRef](#)] [[PubMed](#)]
26. Wang, W.H. Correlation between relaxations and plastic deformation, and elastic model of flow in metallic glasses and glass-forming liquids. *J. Appl. Phys.* **2011**, *110*, 053521.
27. Pugh, S.F. XCII. Relations between the elastic moduli and the plastic properties of polycrystalline pure metals. *Lond. Edinb. Dublin Philos. Mag. J. Sci.* **1954**, *45*, 823–843. [[CrossRef](#)]
28. Li, W.-B.; Li, K.; Fan, K.-Q.; Zhang, D.-X.; Wang, W.-D. Temperature and pressure dependences of the elastic properties of tantalum single crystals under <100> tensile loading: A molecular dynamics study. *Nanoscale Res. Lett.* **2018**, *13*, 118. [[CrossRef](#)]
29. Babicheva, R.I.; Bukreeva, K.A.; Dmitriev, S.V.; Zhou, K. Discontinuous elastic strain observed during stretching of NiAl single crystal nanofilms. *Comput. Mater. Sci.* **2013**, *79*, 52–55. [[CrossRef](#)]
30. Sutrar, V.K.; Mahapatra, D.R. Asymmetry in structural and thermo-mechanical behavior of intermetallic NiAl nanowire under tensile/compressive loading: A molecular dynamics study. *Intermetallics* **2010**, *18*, 1565–1571. [[CrossRef](#)]